CRYSTAL GROWTH & DESIGN
2008
VOL. 8, NO. 11
4165–4172

# Room Temperature Ionic Liquids Assisted Green Synthesis of Nanocrystalline Porous $SnO_2$ and Their Gas Sensor Behaviors

Le-Le Li,[†] Wei-Ming Zhang,[#,‡] Quan Yuan,[†] Zhen-Xing Li,[†] Cheng-Jie Fang,[†] Ling-Dong Sun,[†] Li-Jun Wan,[‡] and Chun-Hua Yan*,[†]

*Beijing National Laboratory for Molecular Sciences, State Key Laboratory of Rare Earth Materials Chemistry and Applications & PKU-HKU Joint Laboratory in Rare Earth Materials and Bioinorganic Chemistry, Peking University, Beijing 100871, China, Beijing National Laboratory for Molecular Science, Institute of Chemistry, Chinese Academy of Sciences (CAS), Beijing 100080, China, and Graduate School of Chinese Academy of Sciences (CAS), Beijing 100049, China*

*Received June 27, 2008; Revised Manuscript Received July 28, 2008*

**ABSTRACT:** Nanocrystalline porous tin dioxide ($SnO_2$) materials have been obtained employing room temperature ionic liquids (1-hexadecyl-3-methylimidazolium bromide, $C_{16}$MimBr) as a template via a green sol−gel method at ambient temperature followed by a suitable thermal treatment. These materials have been thoroughly characterized by X-ray diffraction (XRD), transmission electron microscopy (TEM), high-resolution TEM (HRTEM), X-ray photoelectron spectroscopy (XPS), Raman spectroscopy, FTIR, and nitrogen adsorption−desorption. A careful tuning of heat-treatment procedures allowed the preparation of $SnO_2$ functional materials with Brunauer−Emmett−Teller surface areas ranging from 38 to 140 $m^2\ g^{-1}$, an average pore size between super-micropore (1−2 nm) and mesopore (10 nm) range, and a mean particle size from 3.0 to 10.0 nm. The applications in gas sensors for the nanostructures reveal that the obtained $SnO_2$ materials exhibit highly sensitive, fast-responding, reproducible, and size selective sensing behaviors. The sensor characteristics were discussed in relation to the architectures of the materials, which disclose that the gas-sensor properties are strongly structure-dependent.

## Introduction

$SnO_2$, an *n*-type semiconductor with a stable wide-band gap of 3.8 eV, is a promising key functional material for a wide range of practical applications as excellent gas sensors,[1] solar cells,[2] catalysts,[3] electrode materials,[4] electrochromic windows,[5] and so forth. It is well-known that the performance of this material is influenced by morphological and nanostructure features of the $SnO_2$ crystals, including particle size, shape, surface/volume ratio, and porosity. Thus, to enhance the sensing activity and widespread application of $SnO_2$, much more attention has been focused on controling the size and shape of primary particles as well as manipulating their arrangement and network structure. In particular, porous $SnO_2$ nanostructures could have additional advantages in enhancing the sensor or catalytic activities because such structures can potentially not only have high surface area but can also supply more efficient transport for the reactant molecules to get to the active sites.[3a]

A variety of chemical techniques have been proposed to prepare nanocrystalline $SnO_2$ particles.[6−9] Toupance et al. prepared nanocrystalline mesoporous tin dioxide through the controlled hydrolysis of dialkoxydi($\beta$-diketonato) tin complexes followed by a thermal treatment. A careful tuning of both hydrolysis ratio and calcination temperature enabled the as-prepared materials with surface areas ranging from 50 to 150 $m^2 \cdot g^{-1}$, and a mean particle size between 6 and 18 nm.[10] Recently, the same group demonstrated another preparation of nanocrystalline porous $SnO_2$ with a particle size of 5 to 25 nm, using organically bridged ditin hexaalkynides as precursors.[11] A solution approach was employed by Xin et al. using $SnCl_2 \cdot H_2O$ as starting materials heated in ethylene glycol via a reflux process. The obtained $SnO_2$ nanoparticles were employed to synthesize carbon-supported $PtSnO_2$ catalyst, and it exhibits high promoting catalytic activity for ethanol electrooxidation.[12] Fujihara et al. used a hydrothermal route to prepare mesoporous $SnO_2$ nanocrystallines with an average particle size of ∼4 nm. The resulting porous $SnO_2$ nanoparticles showed good thermal stability, and the specific surface area was more than 110 $m^2 \cdot g^{-1}$ after annealing.[13] Most recently, Yeh et al. also used a hydrothermal process to fabricate nanocrystalline $SnO_2$ particles with a size of ∼3 nm, which exhibited good sensitivity to alcohol.[14]

Ionic liquids (ILs) have been widely studied as a new kind of reaction media owing to their unique properties such as low volatility, nonflammability, high chemical and thermal stabilities, designable structures, high ionic conductivity, broad electrochemical windows, etc.[15] Most recently, ILs have attracted increasing interest as templates or cosolvent systems for the fabrication of nanostructured inorganic materials, since ILs possess tunable solvent properties so that they can easily interact with various surface and chemical reaction environments.[16−24] Various metallic nanoparticles, such as palladium,[17a] iridium,[17b] and germanium nanoparticles[17c] have been prepared in ILs. Gold nanoparticles were synthesized in an ionogel template formed via self-assembly of ILs.[18] Zeolitic materials,[19] mesoporous silica with wormlike porous and highly ordered lamellar structure[20] were prepared with different ILs. Mesoporous $TiO_2$[21,22] and $TiO_2$ nanocrystals[23] were prepared in ILs. Most recently, Chen et al. demonstrated a novel route for preparation of semiconductor ZnO nanocrystals stabilized by IL components, which show tunable photoluminescence and high thermal stability.[24] In contrast, an exploration of ILs' potential in the synthesis of metal oxide nanocrystallines has just begun.

In this work, we present a green and facile synthesis of nanocrystalline porous tin oxide ($SnO_2$) based on the use of one kind of room-temperature ionic liquids (1-hexadecyl-3-methylimidazolium bromide, $C_{16}$MimBr) as a template. A careful tuning of calcination temperature allowed the preparation of $SnO_2$ functional materials with Brunauer−Emmett−Teller

* Corresponding authors. Fax: +86-10-6275-4179; e-mail: yan@pku.edu.cn.
[†] Peking University.
[‡] Institute of Chemistry, Chinese Academy of Sciences (CAS).
[#] Graduate School of Chinese Academy of Sciences (CAS).

10.1021/cg800686w CCC: $40.75 © 2008 American Chemical Society
Published on Web 09/24/2008

surface areas ranging from 38 to 140 $m^2 \cdot g^{-1}$, an average pore size between super-micropore (1−2 nm) and mesopore (10 nm), and a mean particle size from 3.0 to 10.0 nm. This approach is useful for developing nanoprecision oxide materials and provides an effective means to examine the influence of morphological and nanostructural features on sensor properties. The performance in gas sensors for the obtained nanocrystalline porous $SnO_2$ was measured for $H_2$ and CO, and the sensor characteristics were discussed in relation to the nanostructures of the materials. The highly sensitive, fast-responding, reproducible and size selective sensing behaviors of the $SnO_2$ materials, promising their potential applications in shape selective sensor and catalysis.

## Experimental Section

**Preparation of Nanocrystalline Porous $SnO_2$.** All chemicals used were analytical grade and used without further purification. 1-Hexadecyl-3-methylimidazolium bromide ($C_{16}$MimBr) was prepared by the literature method.[20c] Tin chloride pentahydrate ($SnCl_4 \cdot 5H_2O$) was purchased from Beijing Chemical Reagent Company and used as tin precursor without further purification.

In a typical experiment to synthesize nanocrystalline porous $SnO_2$, 5 g of $C_{16}$MimBr was added in a mixed solvent of alcohol (20 mL) and water (50 mL) to form a clear homogeneous solution. Afterward, 3.0 g of $SnCl_4 \cdot 5H_2O$ diluted with 25 mL deionized water was slowly added to the above solution. After the sample was agitated vigorously for 4 h, the product was aged at room temperature for 3 days. The final precipitates were filtered and washed with distilled water, dried at ambient temperature, and extracted with hot alcohol for 48 h. Finally, the product was annealed at 300, 400, and 500 °C in air for 2 h at a ramping rate of 1 $°C \cdot min^{-1}$.

**Characterization.** X-ray powder diffraction (XRD) patterns of the samples were recorded on a Rigaku D/max-2000 X-ray powder diffractometer (Japan) using Cu K$\alpha$ ($\lambda$ = 1.5405 Å) radiation. TEM images were taken on the Hitachi H-9000 NAR transmission electron microscope under a working voltage of 300 kV. High-resolution TEM (HRTEM) was performed on a Philips Tecnai F30 FEG-TEM (USA) operated at 300 kV. The laser Raman spectra were recorded using a Jobin-Yvon HR800 Raman spectrometer (France) with a 30 mW Ar ion laser (488.0 nm). The exposition time is 10 s and accumulates two times. X-ray photoelectron spectrometer (XPS) measurements were carried out in an ion-pumped chamber (evacuated to $2 \times 10^{-9}$ Torr) of an Escalad5 (U.K.) spectrometer, employing Mg K$\alpha$ radiation (BE = 1253.6 eV). IR spectra were recorded on a Nicolet Magna-IR 750 spectrometer equipped with a Nic-Plan Microscope. The nitrogen adsorption and desorption isotherms at 78.3 K were measured using an ASAP 2010 analyzer (Micromeritics Co. Ltd.). The Brunauer−Emmett−Teller (BET) method was utilized to calculate the specific surface areas (SBET) using adsorption data in a relative pressure range from 0.08 to 0.25. With the Barrett−Joyner−Halenda (BJH) model, the pore size distributions were derived from the absorption or desorption branches of the isotherms.

**Measurement of Gas-Sensing Properties.** Sensor test was conducted on a self-building sensor platform. Sensitive materials were dispersed in deionized water and dropped to UST micro heat plate devices to form a thick film with a thickness of about 5 $\mu$m. Synthetic air and specific standard gas ($H_2$ or CO) with various concentrations (diluted in synthetic air) were delivered to the test chamber (with an inner volume of about 30 mL) by Mass Flow Controllers (MFCs) at the same time at a constant total rate of 200 sccm. The sensor devices were heated by an Agilent E3640A programmable DC power supply, and the resistances of the sensitive layers were acquired by a Keithley 2400 source meter. All experiments were carried out at 300 °C after a warm-up process at the same temperature for about an hour.

## Results and Discussion

In conventional solution syntheses the nanostructures of inorganic materials are induced by hydro(or solvo)thermal treatment or assistance of additional organic solvents in a sealed autoclave. In contrast, the key step in this synthetic method to fabricate the nanostructured $SnO_2$ was the process with the assistance of ILs in an open container at ambient pressure. Furthermore, the room-temperature imidazolium ionic liquids (RTILs) used for the formation of the nanostuctures are recyclable through a simple extraction process. This is very crucial for "green chemistry". X-ray diffraction (XRD) measurements were conducted to identify the overall phase compositions of the resulting $SnO_2$ particles, as seen in Figure 1. The peak positions in all the samples match with the diffraction of the tetragonal $SnO_2$ with a cassiterite structure (JCPDS Card No 41-1445). Peaks are quite broad, which demonstrates the nanometric-grained nature of the $SnO_2$ particles. In addition, a progressive increase in peak intensity coupled with a decrease of the peak width was observed as the annealed temperature was increased, indicating an increase in crystallinity of the $SnO_2$ materials. The well-known Scherer crystallite size calculated using the XRD pattern was 3.0, 5.5, and 10.0 nm with annealed temperatures of 300, 400, and 500 °C, respectively, which agreed well with the results observed with TEM as described later.

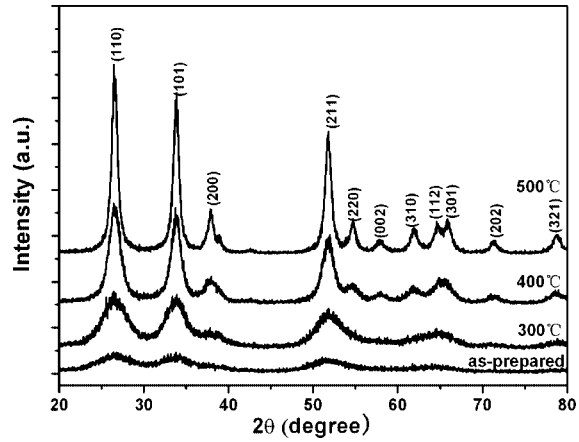


**Figure 1.** XRD patterns of the as-prepared $SnO_2$ sample and the samples annealed at various temperatures.

TEM was utilized to observe the different morphologies of the nanostructured $SnO_2$ samples. Figure 2a shows a representative TEM image of the $SnO_2$ sample calcined at 300 °C, from which a network of assembled nanoparticles of 2−4 nm with uniformly distributed wormhole-like pores of 1−2 nm is observed. The wormhole-like structure is best described as one-dimensional rod-type micelles entangled in a three-dimensional manner. As a result, this structure provides an isotropic porous structure with easily accessible pore openings from any direction, which makes this structure highly desirable for various electrochemical and photoelectrochemical applications.[25] Indeed, the low-angle XRD pattern of the sample shows a broader primary peak which further confirms a short-range ordered pore network of assembled nanoparticles (Supporting Information, Figure S1).[26] High-resolution TEM (HRTEM) images show the lattice images for all the samples (Figure 2b,d,f). The distance between the adjacent lattice fringes corresponds to the interplanar distance of the tetragonal $SnO_2$ (110), which is $d_{110}$ = 0.335 nm. This was further confirmed from the selected area electron diffraction pattern (inset of Figure 2a) shown for the sample calcined at 300 °C. In this electron diffraction pattern bright diffraction rings for various crystalline planes were quite clear, which could be attributed to the crystalline nature of the materials. Not surprisingly, the $SnO_2$ particle sizes increased as the temperature of the thermal treatment was raised from 300 to 500 °C, which corroborated the same trends as those

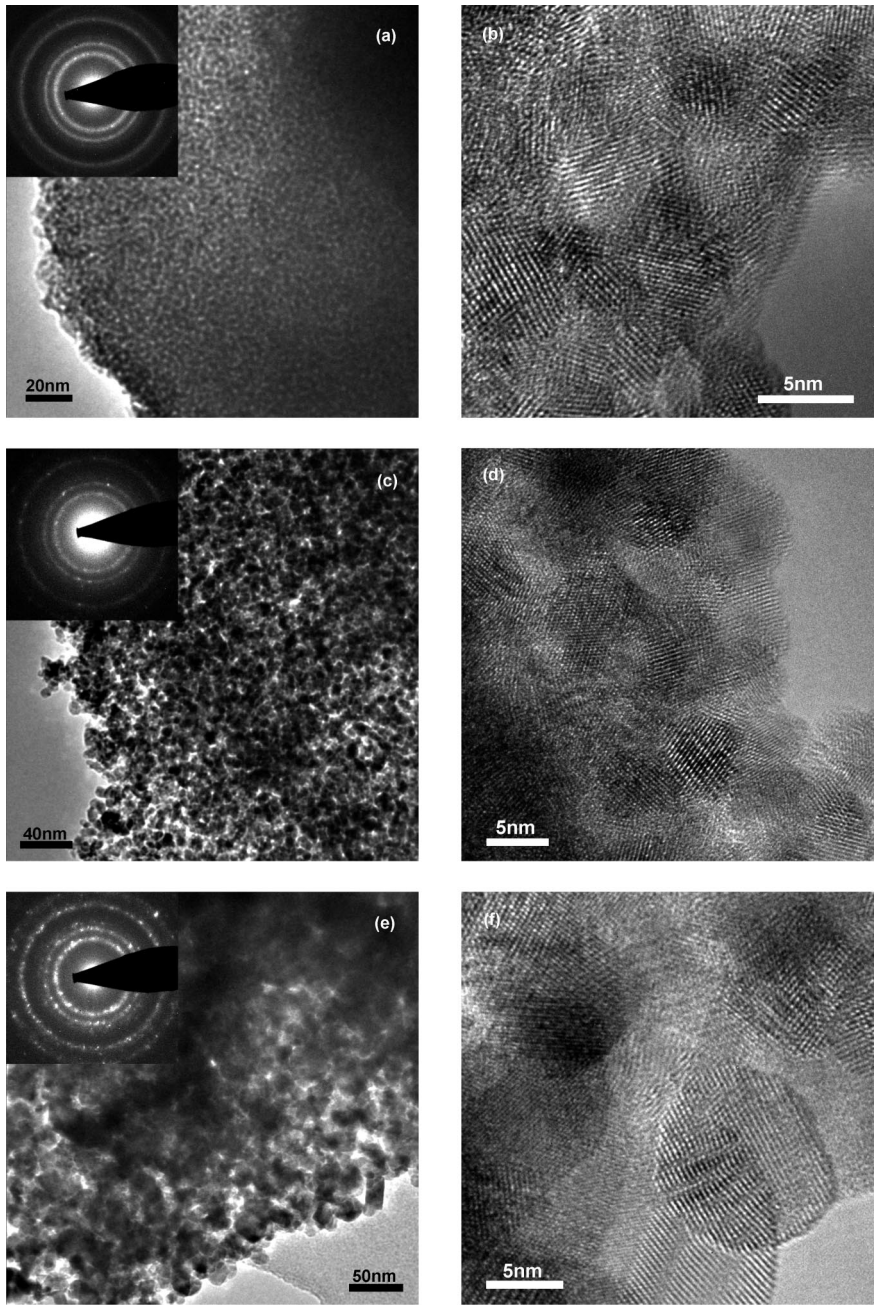


**Figure 2.** TEM images of the nanostructured $SnO_2$ annealed at (a) 300 °C, (c) 400 °C, and (e) 500 °C. HRTEM images of the nanostructured $SnO_2$ annealed at (b) 300 °C, (d) 400 °C, and (f) 500 °C. Insets are the electron diffraction patterns of the respective samples.

deduced from X-ray line sharpening. The crystalline nature of these two samples was also further confirmed from the electron diffraction patterns (inset of Figure 2c,e). It is clear that their pores remain fairly uniformly distributed but become farther apart (Figure 2c,e), as compared with the sample annealed at 300 °C. As the heat-treatment temperature is higher, the pores become larger in size because of the particle growth, and the porous structure tends to be replaced with a more disordered porous network of aggregated nanoparticles.[10,11]

Figure 3 presents Raman spectra of nanocrystalline porous $SnO_2$ with different treatment temperatures. The XRD usually shows the information related to the long-range symmetry of the structure, while the Raman spectrum provides the local symmetry of the chemical bond. The broadband at 550 $cm^{-1}$ corresponds to surface modes,[27] and the intense bands at 631 and 772 $cm^{-1}$ correspond to the modes with $A_{1g}$ and $B_{2g}$ symmetry, respectively. $A_{1g}$ and $B_{2g}$ are related to the expansion and contraction vibration modes of Sn−O bonds in tetragonal $SnO_2$, which usually appear in large single crystals or bulk polycrystalline $SnO_2$, while the broadband at 550 $cm^{-1}$, being related to the facet surface area of a crystal, arise from nanoscale $SnO_2$ with small grain size.[28,29] The spectra of the samples calcined at higher temperature also exhibit four abnormal Raman lines at 472, 504, 550, and 685 $cm^{-1}$. These vibration modes can be reasonably assigned to $E_g$ (472 $cm^{-1}$), $A_{2u}$ (TO) (504 $cm^{-1}$), $A_{2u}$ (LO) (685 $cm^{-1}$) IR-active, and $B_{1u}$ (550 $cm^{-1}$) Raman forbidden modes.[29] It is considered that the presence of IR modes and other forbidden Raman modes is attributed to the decreases of crystal size to the nanoscale (limiting vibrations to the size of the crystal) and to the increases of structural distortions (reducing crystal symmetry).[27,28] Those bands, being related to the facet surface area of a crystal, agree very well

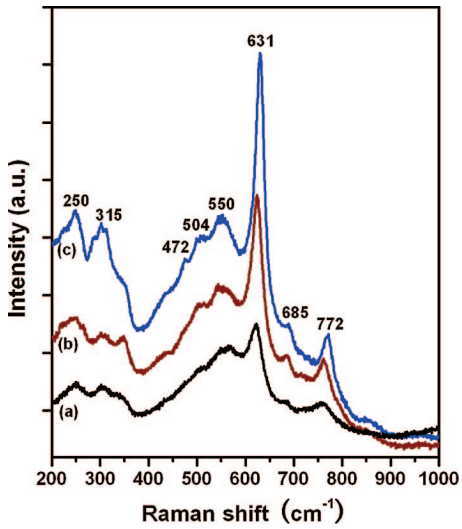


**Figure 3.** Raman spectra of the nanostructured $SnO_2$ annealed at (a) 300 °C, (b) 400 °C, and (c) 500 °C.

with the Matossi force constant model.[30] In addition, two bands at 250 and 315 $cm^{-1}$ were observed. These two bands appear as a single broad feature composed of at least two components in the heat-treated powders. The appearance of these bands has occasionally been reported, while the origin of the bands is not yet elucidated.[31] Yu et al.[31a] assigned Raman bands at 327 $cm^{-1}$ to the confinement effect of photons in one-dimensional chains composed of aggregated fine $SnO_2$ particles. Liu et al.[31b] assigned the Raman bands located at region 210−240 $cm^{-1}$ of rutile $SnO_2$ nanorods to $E_u$ (TO) and $E_u$ (LO) active modes. Since the three-dimensional (3D) aggregation of crystalline tiny nanoparticles is observed in the materials obtained here, it is reasonable to assign these bands to active mode from the inactive $E_u$ mode induced by size effect. Nevertheless, more work is still needed to clarify the origin of these bands in nanostructured $SnO_2$. The Raman bands further confirm the characteristics of the tetragonal structure as well as the nanoparticles with very small size of the obtained $SnO_2$ materials, in agreement with the results deduced from XRD and TEM analysis.

To further characterize the product, XPS was carried out to investigate the surface compositions and chemical states of the products. Figure 4a,b exhibits the high-resolution XPS spectra corresponding to Sn 3*d* and O 1*s* for the nanocrystalline porous $SnO_2$ annealed at various temperatures. All the samples appeared as a spin−orbit doublet at ∼486 eV ($3d_{5/2}$) and ∼495 eV ($3d_{3/2}$), which was in agreement with the reported value in the literature.[32] In the case of the O 1*s* peaks, a shoulder at ∼532 eV is observed with the main peak at ∼531 eV. The main peak is assigned to the lattice oxygen, and the shoulder is due to the oxygen of the Sn-OH bonds.[33,34] The O 1*s* peaks were therefore fitted with two Gaussian functions for comparison. An overall decrease of the $OH^-/O^{2-}$ integrated-intensity ratios with the calcination temperature was observed, which can be explained by the decrease of the hydroxyl groups, resulting from the growth of the nanoparticles and a decrease of the surface area.

The porosity of the $SnO_2$ materials was distinctly confirmed by the analysis of the $N_2$ adsorption−desorption isotherms. Nitrogen adsorption−desorption isotherms of the samples annealed at various temperatures are shown in Figure 5. The materials calcined at 300 °C displays the isotherm of type I according to the IUPAC classification, corresponding to a microporous structure with pore sizes less than 2 nm. The Barrett−Joyner−Halenda (BJH) analysis shows a special Brunauer−Emmett−Teller (BET) surface area of 140 $m^2/g$. The samples mainly contain primary micropores within the range of 1−2 nm, which is in agreement with the results revealed by TEM photographs. DFT calculations fit very well with these values.[35,36] This thickness of the pores indicates that the long-tail ILs are packed in an interdigitated conformation.[20b,c] The materials in this super-microporous (pore size 1−2 nm) range are greatly important, since they bridge the gap between microporous zeolites and mesoporous materials.[37] Such materials exhibit the potential of size and shape selectivity for those organic molecules that are too large to access to the pores of zeolites. While for mesoporous materials, size selectivity is also hard to be observed, since most of the products of sensing or catalytic reactions are much smaller in size than the mesopores.[20c] Nonetheless, the materials calcined at higher temperatures (400 and 500 °C) exhibit pure type IV isotherms with a type H2 hysteresis loop, signifying the mesoporous structure. The presence of a pronounced hysteresis loop in the isotherm curve is indicative of the pores in a 3D intersection network.[38] However, for the sample annealed at 400 °C, this H2 hysteresis loop occurs at $P/P_0 = 0.40-0.42$, which prevented the use of the classical BJH model based on the analysis of the desorption branch of the $N_2$ adsorption isotherm to estimate the pore size distribution of the sample.[10,35] So the overall pore size distribution of the sample was evaluated from the adsorption branch, which was more valid in such systems.[10,11,35] As revealed from the BJH pore size distribution, the average mesopore size is increased to be about 6 and 10 nm, respectively. The BET analysis indicates that the surface area was reduced to 80 and 38 $m^2/g$, respectively. As the heat-treatment temperature is higher, the materials are transformed to be composed of a porous network of aggregated nanoparticles with a mesoporosity arising from the interparticle space because of the annealing process that comprises crystallization, sintering, and growth of the $SnO_2$ particles.[10,11,13] The large surface areas and narrow pore size distributions combined with tailorable pore sizes enhance the potential applications of these nanostructured tin oxides in gas sensor.

Under this synthetic condition, $C_{16}$MimBr played a crucial role of template in forming the nanostructure of $SnO_2$. To better understand the formation process of the nanocrystalline porous $SnO_2$ network, FTIR analyses were carried out on the original ILs, IL/$SnO_2$ hybrid, and the $SnO_2$ sample calcined at 300 °C (Figure 6). The strong peaks around 2851 and 2916 $cm^{-1}$ belonging to the alkyl chain of ILs are still present and do not shift in the spectrum of the hybrid, which indicate that the ILs was entrapped in the $SnO_2$ network and cannot be fully extracted.[39] A broadband corresponding to the Sn-OH vibration band at around 3400 $cm^{-1}$ is superimposed with these stretching signals of the alkyl chain. Below 750 $cm^{-1}$, the intense bands appearing in both the hybrids and the calcined $SnO_2$ at lower frequencies of around 660 $cm^{-1}$ are typical of the Sn−O−Sn asymmetric and symmetric vibrations.[40] In a manner similar to ILs-templated formation mechanism of mesoporous silica,[20] the porous structure of $C_{16}$MimBr/$SnO_2$ hybrid was formed though hydrogen bonding between $C_{16}$MimBr and tin hydroxide as well as $\pi$-$\pi$ stacking of imidazolium rings. As shown in the spectra Figure 6a,b, the two characteristic bands of the imidazolium ring around 3062 and 3082 $cm^{-1}$, which correspond to the symmetric and asymmetric stretch of the HCCH bond in positions four and five of the imidazolium ring,[41] are found to be considerably broadened and shifted to 3108 and 3137 $cm^{-1}$. These effects already demonstrate a strong interaction between the

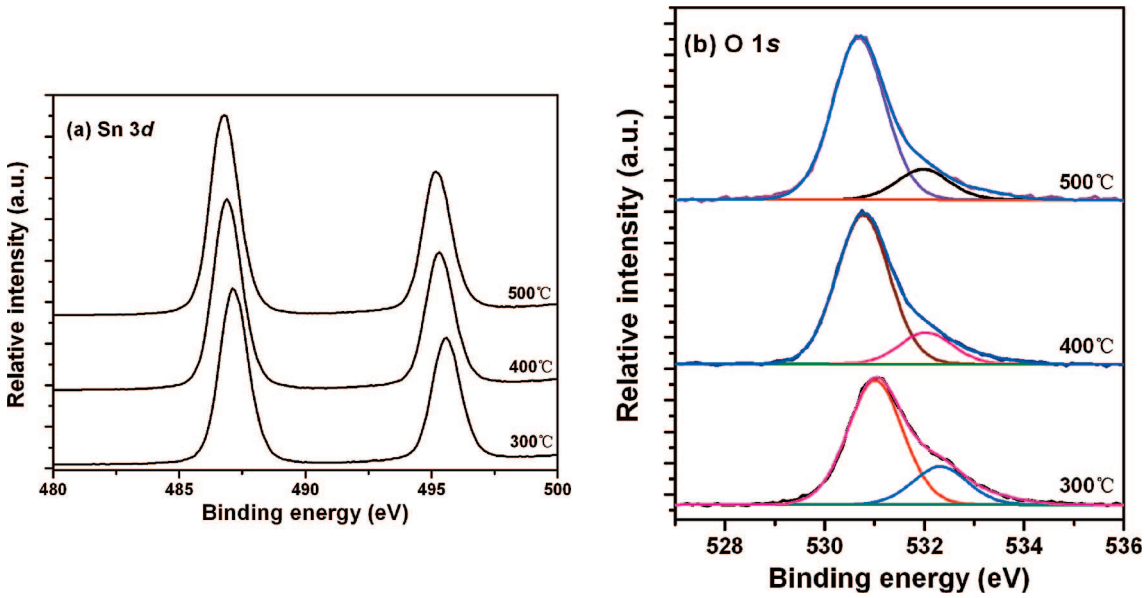


**Figure 4.** (a, b) XPS profiles of the Sn-based nanostructures annealed at various temperatures.

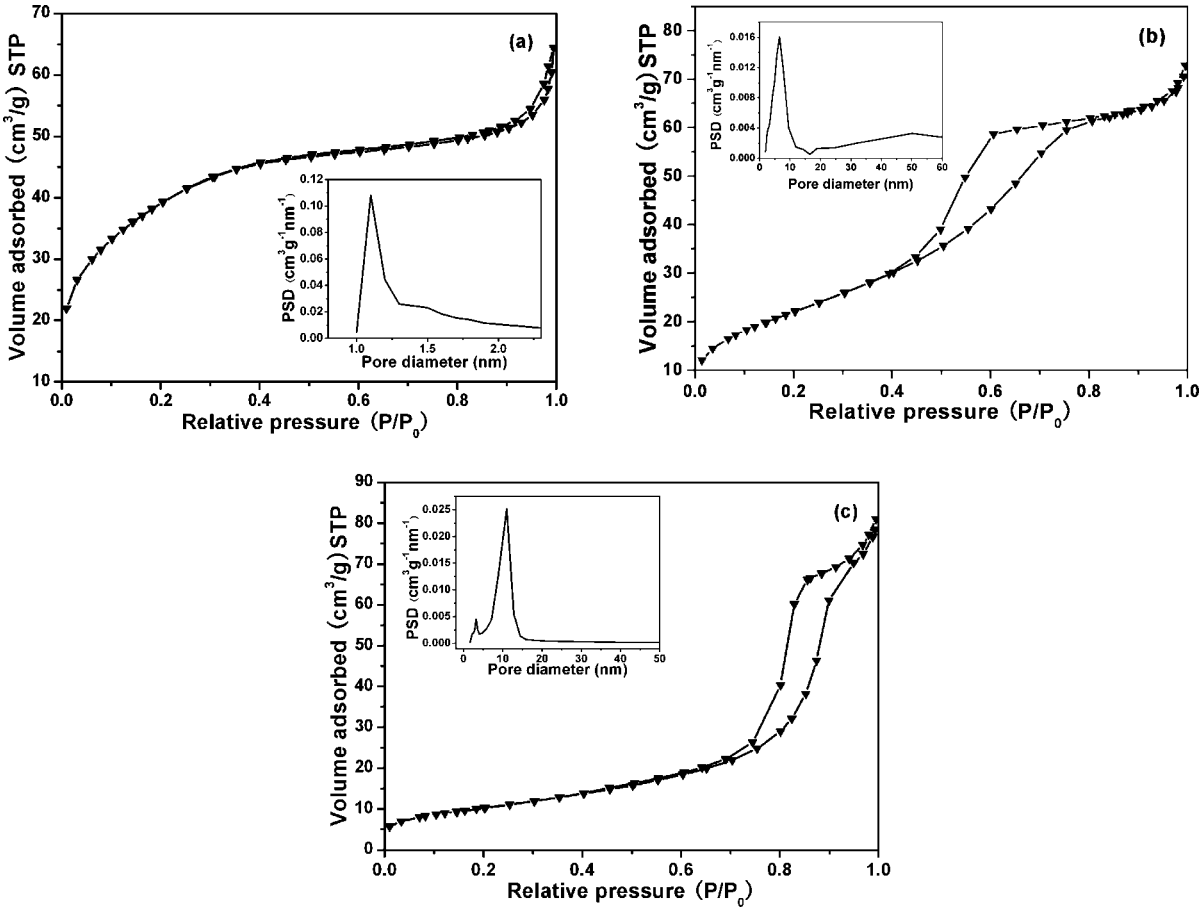


**Figure 5.** Nitrogen gas adsorption−desorption isotherms and pore-size distribution (inset) of the nanostructured $SnO_2$ annealed at (a) 300 °C, (b) 400 °C, and (c) 500 °C.

imidazolium headgroup and the inorganic matrix. In addition, the peak position shifts of the C−N stretching vibration ($\upsilon_{C-N}$) mode of the imidazolium ring at 1178 $cm^{-1}$ toward low wavenumbers (1161 $cm^{-1}$) further confirm the $\pi$-$\pi$ stacking of imidazolium rings.[20a] The reorganizing process of inorganic crystallites via $\pi$-$\pi$ stacking as well as hydrogen bonding significantly influenced the other peaks related to the imidazolium ring and anion of $C_{16}$MimBr in the IR spectra. In the spectrum of the IL/$SnO_2$ hybrid, it is noted that the two bands at 3479 and 3432 $cm^{-1}$ appearing in the spectrum of the pure IL are absent.[42] These two bands can be assigned to the asymmetric $\upsilon_3$ and symmetric $\upsilon_1$ stretching modes of water, where the water interacts with the anion via H-bonding in a symmetric complex.[43] The proposed hydrogen-

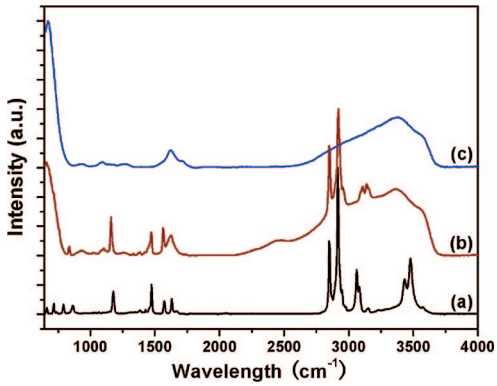


**Figure 6.** FT-IR spectra of (a) $C_{16}$MimBr, (b) $C_{16}$MimBr/$SnO_2$ hybrid, and (c) the $SnO_2$ sample calcined at 300 °C.

bond-*co*-$\pi$-$\pi$-stack mechanism responsible for the formation of the network of porous nanocrystalline, however, still needs further study.

Most recently, Bhaumik et al. demonstrated a preparation of meso- and supermicroporous $SnO_2$ particles by using an anionic surfactant, sodium dodecylsulfate, and a special Schiff base, respectively, as templates. And the resulting nanoporous $SnO_2$ materials exhibited rather high specific surface area up to 555 $m^2 \cdot g^{-1}$.[44] In comparison with these two templates, which directed the assembly of the mesostructures through electrostatic and coordination interactions, respectively, the structure-directing agent (ILs) with hydrophobic regions and a high directional polarizability used here directed the formation of the meostructure through the hydrogen-bond-*co*-$\pi$-$\pi$-stack mechanism. Since it was proven that the surfactant packing, which is the dominant factor in determining the final structure (mesophase, pore size, surface area, etc.) of the mesoporous materials, depends on the molecular geometry of the surfactants (such as the size or charge of the polar headgroup, the number of carbon atoms in the hydrophobic chain, the molecular shape and so forth),[45] it is reasonable to deduce that the different amphiphile templates used are the key factor for the assembly of resulting mesostructures with various surface areas. This example also suggests that the proper choice of templates for the assembly will obviously be important in the production of mesostructures with improved structural and functional properties.

The gas-sensing properties of the obtained nanocrystalline micro/mesoporous $SnO_2$ (P1, P2, and P3: pore size = 1−2, 6.0, 10.0 nm, respectively) have been investigated. Figure 7 shows the sharp variation of the sensor resistance to different concentrations of the target gases ($H_2$ or CO) at the operating temperature of 300 °C in synthetic air. The sensing mechanism is based on surface reactions with gases in the atmosphere that cause a change in the semiconductor's resistance due to charge transfer between the adsorbate and the adsorbent. The resistance ($R_a$) of the mesoporous $SnO_2$ layers (P2 and P3) in dry air was $10^{6.0-6.2}$ Ω at the tested temperatures, which is close to that of the $SnO_2$ crystallite,[46] while an extremely high resistance ($10^{9.3-9.5}$ Ω) for the microporous $SnO_2$ layers (P1) was observed. It was reported that the resistance of $SnO_2$ sensors in air increased steeply with decreasing the $SnO_2$ crystallite size below 6 nm in diameter, since the whole crystallite is covered with the depletion region under these conditions.[47] Thus, the high resistance of the present sample P1 sensors, in comparison with the sample P2 and P3 sensors, can be reasonably understood from their much smaller crystallite size. Under the present operating conditions, for all the porous $SnO_2$ sensors, it is noticed that the sensor resistance decreases with increasing

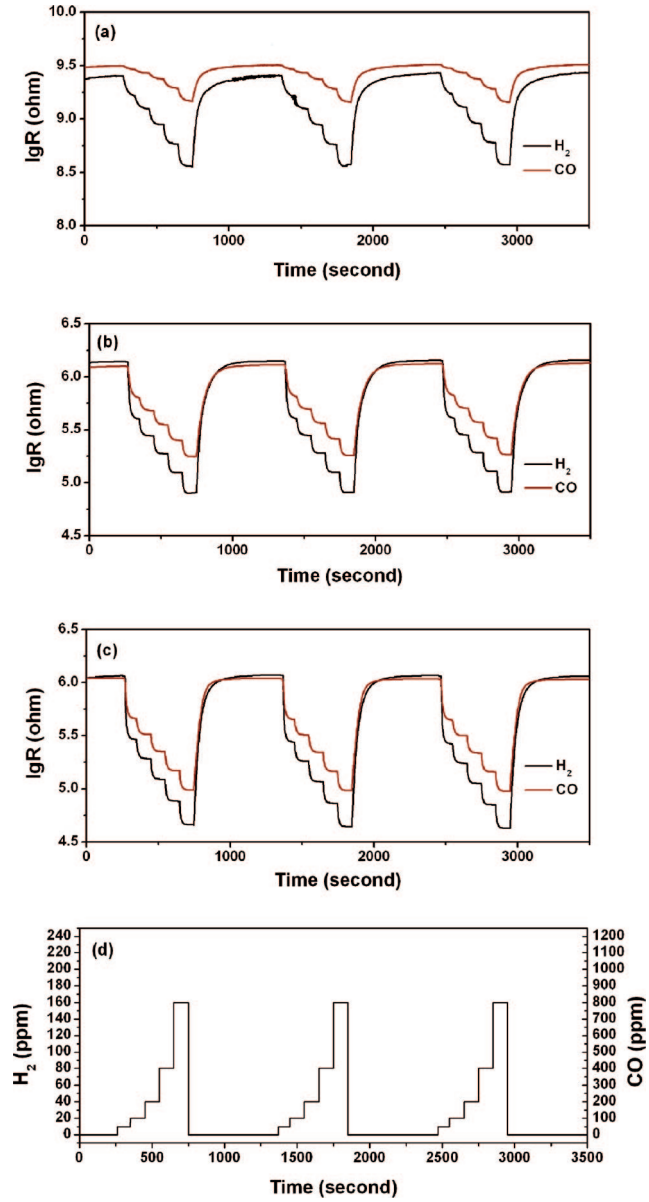


**Figure 7.** Gas-sensing response and recovery transients of the nanostructured $SnO_2$ with different pore architectures: (a) P1, pore size = 1−2 nm, (b) P2, pore size = 6.0 nm, and (c) P3, pore size = 10.0 nm, (d) to switching-on and -off various concentrations of the target gases ($H_2$ or CO).

concentration of reducing gas in air. Figure 7 laid out reversible changes in resistance when the surrounding atmosphere is cycled between pure air and different concentrations of the target gases. In all cases, the resistance variation in the presence of the target species was proportional to the analyte concentration, without displaying any saturation effect. The recovery of the air conductance value after sensing tests was almost complete, suggesting the occurrence of reversible interactions between the analytes and the sensor elements. Furthermore, the response and recovery times (time to reach 90% of the total resistance variation) of the composite systems were less than 60 and 180 s (see Table S1 in Supporting Information), respectively, suggesting that the sensors respond quickly to both the introduction and the removal of small amounts of target gases in air. The reversibility and repeatability of these sensors were also satisfactory, as observed by repeating the tests many times without detecting any significant variation in the functional

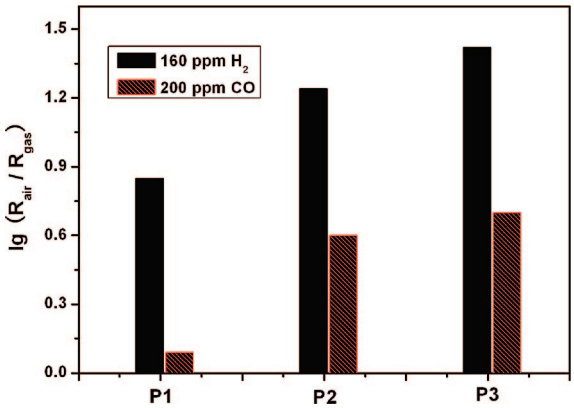


**Figure 8.** Response of the nanostructured $SnO_2$ with different pore sizes (P1: pore size = 1−2 nm, P2: pore size = 6.0 nm, and P3: pore size = 10.0 nm) to selected concentrations of $H_2$ and CO.

response. The high sensitivity to the target gases and rapid response of our $SnO_2$ materials can be attributed to the intrinsically small grain size and high surface-to-volume ratios associated with the accessible porous structures.[1c−e,48]

From Figures 7 and 8 and Table S1 (see Supporting Information), it is interesting to note that the observed resistance variations are systematically higher and faster for mesoporous $SnO_2$ sensor (P2 and P3 sample) with respect to the microporous $SnO_2$ matrices (P1 sample), although a relative lower BET surface areas were observed for P2 and P3 samples. These observations seem to contradict the general trend that higher sensitivity is to be expected for larger surface areas. There are two explanations for the faster response and higher sensitivity of the P2 and P3 samples relative to the P1 sample. First, according to previous reports, the sensitivity to the target gas strongly depends on the ease of diffusion of gas molecules inside the sensitive material.[1c,d,49] It is clear that the gas molecule is diffused most easily inside the deeper region of the mesoporous $SnO_2$ layers (P2 and P3) and reacts with oxygen adsorbed on the surface. It is pretty evident that porosity plays a key role in the efficiency of semiconductor metal oxide gas sensors. This demonstrates that pore size and surface areas are correlated in such sensor materials, with potentially opposite impact. The pores should be wide enough for efficient diffusion of the gas molecules, and the benefit of a high specific surface area must not be thwarted by limitations in the accessibility of the surface. The second is the difference in the charge carrier diffusion rate of the P1, P2, and P3 samples that were annealed at various temperatures. The sample P3 annealed at higher temperature, which showed higher crystallinity and pore interconnectivity, presented a lower potential barrier resulting in the faster transportation of charge carriers from the surface into the bulk and vice versa.[50] This analysis is further confirmed by the fact that the P2 and P3 sensor with different surface area showed similar gas sensitivity. Accordingly, for both the target gases examined in the present work, larger resistance variation and faster response were observed for the samples with lower surface areas, but larger pores and higher crystallinity, which efficiently affect the diffusion of gas molecules and the charge carrier diffusion rate. This example also suggests that a balance between these complementary aspects needs to be chosen for the optimum sensor performance. It is also worth highlighting that the magnitude of the response of the sample P1 sensors toward $H_2$ is much larger than the response to CO, in comparison with that of the sample P2 and P3 at the same test conditions, which suggests that the sample P1 sensors exhibits higher selectivity to smaller $H_2$ molecules. Such differences in the sensing behavior are apparently related to the effects of steric hindrance, imposed by the molecular sizes of the target gases relative to the pore sizes of the $SnO_2$ matrix, on the diffusion and accessibility of the gases to the deeper region of the $SnO_2$ layers. This observed size selectivity of the porous $SnO_2$ materials, together with their controllable pore sizes and highly sensitive and fast-responding sensing behaviors, promising the potential applications in shape selective sensor and catalysis.

## Conclusions

We have developed an easy solution-based method to produce nanocrystalline porous tin dioxide materials, involving the use of the ILs as template. A careful tuning of annealed temperature allowed the preparation of $SnO_2$ functional materials with Brunauer−Emmett−Teller surface areas ranging from 38 to 140 $m^2 \cdot g^{-1}$, an average pore size between super-micropore (1−2 nm) and mesopore (10 nm) range, and a mean particle size from 3.0 to 10.0 nm. The applications in gas sensors for the nanostructures reveal that the obtained $SnO_2$ materials exhibit highly sensitive, fast-responding, reversible and size selective sensing behaviors. The sensor characteristics were discussed in relation to the architectures of the materials, which disclose that the gas-sensor properties are strongly structure-dependent. These results give us a guideline for the study of the size-dependent properties for functional materials as well as further applications for gas sensors. Our synthesis method provides an inexpensive and green wet-chemical route toward tailoring semiconductor metal oxide for the reproducible and sensitive detection of toxic or combustible gases at parts per million levels.

**Acknowledgment.** This work was supported by the MOST of China (2006CB601104), NSFC (10374006 and 20221101) and the Founder Foundation of PKU.

**Supporting Information Available:** Small-angle XRD pattern of the $SnO_2$ samples; table of response and recovery times of the nanostructured $SnO_2$ with different pore sizes to selected concentrations of $H_2$ and CO. This material is available free of charge via the Internet at http://pubs.acs.org.

## References

(1) (a) Ihokura, K.; Watson, J. *The Stannic Oxide Gas Sensor Principles and Applications*; CRC Press: New York, 1994. (b) Varghese, O. K.; Malhotra, L. K. *J. Appl. Phys.* **2000**, *87*, 7457. (c) Wang, Y.; Jiang, X.; Xia, Y. *J. Am. Chem. Soc.* **2003**, *125*, 16176. (d) Huang, J.; Matsunaga, N.; Shimanoe, K.; Yamazoe, N.; Kunitake, T. *Chem. Mater.* **2005**, *17*, 3513. (e) Epifani, M.; Díaz, R.; Arbiol, J.; Comini, E.; Sergent, N.; Pagnier, T.; Siciliano, P.; Faglia, G.; Morante, J. R. *Adv. Funct. Mater.* **2006**, *16*, 1488.
(2) Bergeron, B. V.; Marton, A.; Oskam, G.; Meyer, G. J. *J. Phys. Chem. B* **2005**, *109*, 937.
(3) (a) Zhao, Q.; Zhang, Z.; Dong, T.; Xie, Y. *J. Phys. Chem. B* **2006**, *110*, 15152. (b) Yu, K.; Wu, Z.; Zhao, Q.; Li, B.; Xie, Y. *J. Phys. Chem. C* **2008**, *112*, 2244.
(4) Han, S.; Jang, B.; Kim, T.; Oh, S. M.; Hyeon, T. *Adv. Funct. Mater.* **2005**, *15*, 1845.
(5) Cummins, D.; Boschloo, G.; Regan, M.; Corr, D.; Rao, S. N.; Fitzmaurice, D. *J. Phys. Chem. B* **2000**, *104*, 11449.
(6) Nayral, C.; Ould-Ely, T.; Maisonnat, A.; Chaudret, B.; Fau, P.; Lescouzères, L.; Peyre-Lavigne, A. *Adv. Mater.* **1999**, *11*, 61.
(7) Pang, G.; Chen, S.; Koltypin, Y.; Zaban, A.; Feng, S.; Gedanken, A. *Nano. Lett.* **2001**, *1*, 723.
(8) Wen, Z.; Wang, G.; Lu, W.; Wang, Q.; Zhang, Q.; Li, J. *Cryst.Growth Des.* **2007**, *7*, 1722.
(9) Rumyantseva, M. N.; Gaskov, A. M.; Rosman, N.; Pagnier, T.; Morante, J. R. *Chem. Mater.* **2005**, *17*, 893.
(10) Toupance, T.; Babot, O.; Jousseaume, B.; Vilaça, G. *Chem. Mater.* **2003**, *15*, 4691.

(11) Toupance, T.; Hamzaoui, H. E.; Jousseaume, B.; Riague, H.; Saad-eddin, I.; Campet, G.; Brötz, J. *Chem. Mater.* **2006**, *18*, 6364.
(12) Jiang, L.; Sun, G.; Zhou, Z.; Sun, S.; Wang, Q.; Yan, S.; Li, H.; Tian, J.; Guo, J.; Zhou, B.; Xin, Q. *J. Phys. Chem. B* **2005**, *109*, 8774.
(13) Fujihara, S.; Maeda, T.; Ohgi, H.; Hosono, E.; Imai, H.; Kim, S.-H. *Langmuir* **2004**, *20*, 6476.
(14) Chiu, H. C.; Yeh, C. S. *J. Phys. Chem. C* **2007**, *111*, 7256.
(15) Antonietti, M.; Kuang, D. B.; Smarsly, B.; Zhou, Y. *Angew. Chem., Int. Ed.* **2004**, *43*, 4988.
(16) Parnham, E. R.; Morris, R. E. *Acc. Chem. Res.* **2007**, *40*, 1005.
(17) (a) Deshmukh, R. R.; Rajagopal, R.; Srinivasan, K. V. *Chem. Commun.* **2001**, 1544. (b) Dupont, J.; Fonseca, G. S.; Umpierre, A. P.; Fichtner, P. F. P.; Teixeira, S. R. *J. Am. Chem. Soc.* **2002**, *124*, 4228. (c) Endres, F.; El Abedin, S. Z. *Chem. Commun.* **2002**, 892.
(18) Firestone, M. A.; Dietz, D. L.; Seifert, S.; Trasobares, S.; Miller, D. J.; Zaluzec, N. J. *Small* **2005**, *7*, 754.
(19) (a) Cooper, E. R.; Andrews, C. D.; Wheatley, P. S.; Webb, P. B.; Wormald, P.; Morris, R. E. *Nature* **2004**, *430*, 1012. (b) Parnham, E. R.; Morris, R. E. *Chem. Mater.* **2006**, *18*, 4882.
(20) (a) Zhou, Y.; Schattka, J. H.; Antonietti, M. *Nano Lett.* **2004**, *4*, 477. (b) Zhou, Y.; Antonietti, M. *Adv. Mater.* **2003**, *15*, 1452. (c) Zhou, Y.; Antonietti, M. *Chem. Mater.* **2004**, *16*, 544.
(21) Zhou, Y.; Antonietti, M. *J. Am. Chem. Soc.* **2003**, *125*, 14960.
(22) Li, Y.; Li, J.; Wang, M.; Li, Z.; Liu, H.; He, P.; Yang, X.; Li, J. *Cryst. Growth Des.* **2005**, *5*, 1643.
(23) Ding, K.; Miao, Z.; Liu, Z.; Zhang, Z.; Han, B.; An, G.; Miao, S.; Xie, Y. *J. Am. Chem. Soc.* **2007**, *129*, 6362.
(24) Liu, D. P.; Li, G. D.; Su, Y.; Chen, J. S. *Angew. Chem., Int. Ed.* **2006**, *45*, 7370.
(25) Spray, R. L.; Choi, K. S. *Chem. Commun.* **2007**, 3655.
(26) Bagshaw, S. A.; Prouzet, E.; Pinnavaia, T. J. *Science* **1995**, *269*, 1242.
(27) Hu, J. Q.; Ma, X. L.; Shang, N. G.; Xie, Z. Y.; Wong, W. B.; Lee, C. S.; Lee, S. T. *J. Phys. Chem. B* **2002**, *106*, 3823.
(28) Cheng, B.; Russell, J. M.; Shi, W.; Zhang, L.; Samulski, E. T. *J. Am. Chem. Soc.* **2004**, *126*, 5972.
(29) Peercy, P. S.; Morosin, B. *Phys. Rev. B* **1973**, *7*, 2779.
(30) Matossi, F. *J. Chem. Phys.* **1951**, *19*, 1543.
(31) (a) Yu, K. N.; Xiong, Y.; Liu, Y.; Xiong, C. *Phys. Rev. B* **1997**, *55*, 2666. (b) Liu, Y.; Zheng, C.; Wang, W.; Yin, C.; Wang, G. *Adv. Mater.* **2001**, *13*, 1883.
(32) Ramgir, N. S.; Mulla, I. S.; Vijayamohanan, K. P. *J. Phys. Chem. B* **2005**, *109*, 12297.
(33) Liang, C.; Shimizu, Y.; Sasaki, T.; Koshizaki, N. *J. Phys. Chem. B* **2003**, *107*, 9220.
(34) Moon, T.; Hwang, S. T.; Jung, D. R.; Son, D.; Kim, C.; Kim, J.; Kang, M.; Park, B. *J. Phys. Chem. C* **2007**, *111*, 4164.
(35) Clavier, G. M.; Pozzo, J. L.; Bouas-Laurent, H.; Liere, C.; Rouxb, C.; Sanchez, C. *J. Mater. Chem.* **2000**, *10*, 1725.
(36) Olivier, J. P. *J. Porous Mater.* **1995**, *2*, 9.
(37) (a) Chandra, D.; Bhaumik, A. *Microporous Mesoporous Mater.* **2008**, *112*, 533. (b) Shpeizer, B. G.; Bakhmutov, V. I.; Clearfield, A. *Microporous Mesoporous Mater.* **2006**, *90*, 81.
(38) GreggS. J. SingK. S. W. *Adsorption, Surface Area and Porosity*; Academic: London, 1997; p 111.
(39) Dai, S.; Ju, Y. H.; Gao, H. J.; Lin, J. S.; Pennycook, S. J.; Barnes, C. E. *Chem. Commun.* **2000**, 243.
(40) Jimenez, V. M.; Caballero, A.; Fernandez, A.; Espinos, J. P.; Ocana, M.; Gonzalez-Elipe, A. R. *Solid State Ionics* **1999**, *116*, 117.
(41) Fitchett, B. D.; Conboy, J. C. *J. Phys. Chem.* **2004**, *108*, 20255.
(42) Wang, T.; Kaper, H.; Antonietti, M.; Smarsly, B. *Langmuir* **2007**, *23*, 1489.
(43) Cammarata, L.; Kazarin, S. G.; Salter, P. A.; Welton, T. *Phys. Chem. Chem. Phys.* **2001**, *3*, 5192.
(44) Chandra, D.; Mukherjee, N.; Mondal, A.; Bhaumik, A. *J. Phys. Chem. C* **2008**, *112*, 8668.
(45) (a) Tolbert, S. H.; Landry, C. C.; Stucky, G. D.; Chmelka, B. F.; Norby, P.; Handon, J. C.; Monnier, A. *Chem. Mater.* **2001**, *13*, 2256. (b) Monnier, A.; Schüth, F.; Huo, Q.; Kumar, D.; Margolese, D.; Maxwell, R. S.; Stucky, G. D.; Krishnamurty, M.; Petroff, P.; Firouzi, A.; Janicke, M.; Chmelka, B. F. *Science* **1993**, *261*, 1303.
(46) Baik, N. S.; Sakai, G.; Miura, N.; Yamazoe, N. *Sens. Actuators, B* **2000**, *63*, 74.
(47) (a) Xu, C.; Tamaki, J.; Miura, N.; Yamazoe, N. *Chem. Lett.* **1990**, *1990*, 441. (b) Hyodo, T.; Abe, S.; Shimizu, Y.; Egashira, M. *Sens. Actuators, B* **2003**, *93*, 590.
(48) (a) Wu, N. L.; Wang, S. Y.; Rusakova, I. A. *Science* **1999**, *285*, 1375. (b) Soulantica, K.; Erades, L.; Sauvan, M.; Senocq, F.; Maisonnat, A.; Chaudret, B. *Adv. Funct. Mater.* **2003**, *13*, 553.
(49) Matsunaga, N.; Sakai, G.; Shimanoe, K.; Yamazoe, N. *Sens. Actuators, B* **2002**, *83*, 216.
(50) Shirahata, N.; Shin, W.; Murayama, N.; Hozumi, A.; Yokogawa, Y.; Kameyama, T.; Masuda, Y.; Koumoto, K. *Adv. Funct. Mater.* **2004**, *14*, 580.

CG800686W